# Eddy Current Microsensor and RBF Neural Networks for Detection and Characterization of Small Surface Defects

Chifaa Aber[1], Azzedine Hamid[2], Mokhtar Elchikh [1], Tierry Lebey [3].

[1] *Physical engineering Department, Applied Power Electronics Laboratory, University of Science and Technology USTO-MB, 31000, Oran, Algeria, aber_ch@hotmail.com*
[2] *Faculty of Electrical Engineering, University of Science and Technology USTO-MB, 31000Oran, Algeria*
[3] *Laplace Laboratory, University of Paul Sabatier, Toulouse Cedex 9, France*

The growing complexity of industrial processes and manufactured parts, the growing need for safety in service and the desire to optimize the life of parts, require the implementation of increasingly complex quality assessments. Among the various anomalies to consider, sub-millimeter surface defects must be the subject of particular care. These defects are extremely dangerous as they are often the starting point for larger defects such as fatigue cracks, which can lead to the destruction of the parts.
Penetrant testing is now widely used for this type of defect, due to its good performance. Nevertheless, it should be abandoned eventually due to environmental standards. Among the possible alternatives, the use of eddy currents (EC) for conductive materials is a reliable, fast, and inexpensive alternative.
The study concerns the design and modeling of eddy current probe structures comprising micro-sensors for non-destructive testing. The moving band finite element method is implemented for this purpose to take into account the movement of the sensor, experimental validations were conducted on a nickel-based alloy specimen. The real and imaginary parts of the impedance at every position of the sensor computed by experiments and simulations were in good agreement. The crack detection quality was quantified and the geometric characteristics of the defects were estimated using RBF NN (Radial Basis Function Neural Networks) that were designed and implemented on the acquired signals.

Keywords: Defect inspection, Eddy current, Finite element method, Microsensor, RBF, Moving band method, Neural network.

## 1. INTRODUCTION

Industrial processes and manufactured parts have become increasingly complex throughout the last century. Non-Destructive Testing (NDT), the last stage of the industrial process, aims to control the quality of industrial parts, in particular mechanical parts, without damaging them. NDT has become an industrial necessity; the failure of these parts can lead to more important consequences.

Many methods are possible to perform the task of NDT [1]-[3]. Among the most commonly used methods, we can cite ultrasound [4], methods using ionizing radiation (radioscopy), magnetoscopy, and Penetrant testing, which is often used, but it is set to disappear due to new standards in terms of pollution. Among the possible replacement solutions, the eddy current technique (EC) is widely used in the field of NDT when it comes to electrically conductive materials [5]-[9]. It represents most of the controls in the field of aeronautics.

The eddy current (EC) investigation is based on a coil fed by a time-harmonic source current used to generate and sense the electrical current in the metallic part simultaneously. The modification of the eddy currents due to the presence of a defect leads to the variation in the magnetic flux density of the coil, these variations allowing the detection of these defects. This method is indeed sensitive to defects in the geometric or electromagnetic state of the material, such as inclusions, cracks, or the effects of corrosion. In addition, it is easy to implement, robust in the context of industrial applications, and relatively inexpensive. However, the growing need for reliability and speed for inspection operations requires the development of new control systems such as microsensor [10]-[12].

The main objective of this paper is the programming of tools allowing to simulate this configuration of NDT by EC which can pose difficulties of modeling. These developments will be integrated into the computer code which is based on a numerical resolution of Maxwell's equations in a 3D harmonic regime using the Finite Element Method (FEM) [13]-[17]. The motion band method was chosen for the economic management of sensor displacement, as well as for taking into account fine domains (microcoil, lift-off zone) without degrading the quality of mesh.

Acquiring EC signals is only the first step in the NDT process. It is then necessary to process the signals acquired to

extract the useful information and transform them into data qualifying the possible faults sought.

The inversion of the signals, or characterization of the defects [18], makes it possible to estimate the geometric characteristics of the defects from the corresponding EC signals: it is a question of solving the "inverse problem". This procedure was carried out by an inversion algorithm which is established and implemented to estimate the geometric parameters of defects using RBF [19] (Radial Basis Function) neural networks.

## 2. SENSOR DESIGN

The eddy current sensor used for the inspection of defects consists of a planar square inductor. In Fig.1., we illustrate a 2D representation of the planar inductor used for this purpose. The inductor is specified by the number of turns n = 5, turn width w = 0.1 mm, turn spacing s = 0.1 mm, and turn thickness t = 0.025 mm, distributed over a total thickness of 1.25 mm, the length of the coil side is c = 2.6 mm.
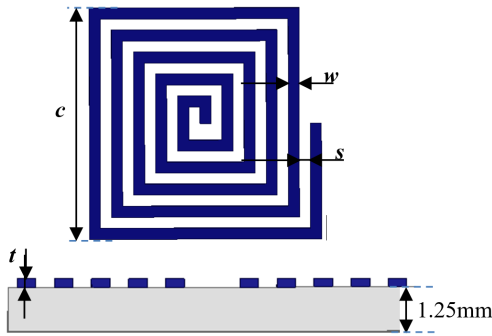


Fig.1. Schematic view of the sensor.

## 3. SENSOR CHARACTERIZATION

In this section, we present the geometrical and electrical characteristics of the planar square inductor.

### A. Geometrical characterization

The proposed sensor is a square integrated inductor whose developed length $l_{tot}$ is calculated by the formula:

$$l_{tot} = \sum_{i=0}^{n-1} 4\left(c - 2(w+s)i\right) \tag{1}$$

The total effective surface $S_{tot}$ of the inductor, which is the equivalent surface of all the turns, is given by:

$$S_{tot} = \sum_{i=0}^{n-1} 4w\left(c - 2(w+s)i\right) \tag{2}$$

Where $n$ is the number of turns, $c$ is the external rib of the coil, s is the inter-lines distance, and w is the line width (Fig.1.).

### B. Electrical characterization

The equivalent electrical model of the integrated inductor [20] is shown in Fig.2. The theoretical model of a coil is an RLC dipole whose impedance is written as:

$$Z = \frac{R + jL\omega}{1 + jRC\omega - LC\omega^2}, \tag{3}$$

Where $\omega$ is the current / voltage pulsation, $L, R$, and $C$ are the inductance, the resistance, and the capacitance of the induction coil, respectively.
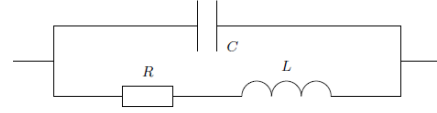


Fig.2. Electrical model of the coil.

The probe impedance with an excited current $I$ at a frequency $f$ can be computed by using the FE modeling [21] developed in section (4). The inductance of the probe is obtained by the following expression:

$$L = \frac{2\,W_m}{I^2}, \tag{4}$$

Where $I$ is the coil excitation current, $W_m$ is the average magnetic energy stored throughout the space defined by the following relation:

$$W_m = R_e\left(\frac{1}{2}\int_\Omega \boldsymbol{b}.\boldsymbol{h}^* d\Omega\right), \tag{5}$$

Where $\boldsymbol{b}$ is the magnetic flux density, $\boldsymbol{h}$ is the magnetic field. The resistance of the coil can be calculated from the power losses in the conductive medium:

$$R = \frac{P_j}{I^2}, \tag{6}$$

with:

$$P_j = \int_{\Omega_c} \frac{1}{\sigma} \|\boldsymbol{j}\|^2 \, d\Omega, \tag{7}$$

Where $\boldsymbol{j}$ is the eddy current density, $\sigma$ is the material conductivity. The total capacitance is expressed as a function of the electrical energy $W_e$ stored in the simulated space and the total voltage $V_{tot}$:

$$C = \frac{2\,W_e}{V_{tot}^2}, \tag{8}$$

with:

$$W_e = \frac{\varepsilon}{2} \int_\Omega \|\boldsymbol{e}\|^2 \, d\Omega, \tag{9}$$

Where $\varepsilon$ is the electric permittivity, $\boldsymbol{e}$ is the electric field,

$\Omega$ is the whole computation area (sensor and air box).

### C. Physical characterization

For a complete qualification of the micro inductor, it is useful to determine its sensitivity and its electrical noise signal if the coil is used as a receiver. In case this element of probes is used as a transmitter, the calculation of the emissive ability is necessary. As the sensor element is used as a transmitter and a receiver, a rigorous and complete study is essential to characterize our sensor.

The sensitivity of a sensor is the ratio of the respective variations of the output quantity (voltage $V$ ) of the sensor and the measurand (magnetic field $b$ ). The sensitivity at frequency $f$ is written as:

$$S = \left| \frac{dV}{db} \right| = 2\pi f S_{tot} . \tag{10}$$

The effective noise voltage of a coil when it is not traversed by a current is written as:

$$v_b = \sqrt{4 k T R \Delta f} , \tag{11}$$

Where $T$ is the temperature, $\Delta f$ is the measuring frequency range, and $k$ is Boltzmann's constant. The effective value of the equivalent magnetic noise is the ratio of the effective noise voltage $v_b$ and the sensitivity:

$$B_b = \frac{v_b}{S} . \tag{12}$$

The emissive ability is the ratio of the emitted field $b$ and the current $I$ required for its emission. Its expression is obtained using that of the magnetic flux produced by an inductance element $L$ crossed by a current $I$, which is written with $b$ assumed to be uniform over the entire effective area of the coil:

$$\Phi = L I = b S_{tot}$$

The emissive ability $P_e$ is given by:

$$P_e = \frac{b}{I} = \frac{L}{S_{tot}} \tag{13}$$

### D. Optimization of the coil

The sensitivity of microcoils is lower and the noise is greater compared to conventional coils. However, these disadvantages are limited by the fact that the noise level is very low for both cases, it is lower than the noise generally provided by the instrumentation and, therefore, not very disturbing. In addition, the thermal noise calculation is carried out over a wide range of frequencies and thus very strongly overestimated.

The miniaturization of microcoils is favorable on several points: The resolution is a priori significantly improved by

microcoils: in fact, it is roughly proportional to the footprint, which is very small for this technology. The emissive ability is inversely proportional to the total effective area, which means that a microcoil will emit a greater field at the same current. The values of the geometrical, electrical, and physical characteristics are summarized in Table 1.

Table 1. Numerical values of the coil characteristics calculated at 800 KHz.

| Parameter | Value |
|---|---|
| Number of turns | 5 |
| External length | 2.6 $mm$ |
| Line width | 100 $\mu m$ |
| Inter-line width | 100 $\mu m$ |
| Developed length | 36 $mm$ |
| Total surface | 17.8 $mm^2$ |
| Capacity $C$ | 79.65 $fF$ |
| Resistance $R$ | 0.28 $\Omega$ |
| Inductance $L$ | 0.023 $\mu H$ |
| Resonant frequency $f_0$ | 1.98 $MHz$ |
| Sensitivity $S$ | 89.42 $V/T$ |
| Noise voltage $v_b$ | 0.214 $\mu V$ |
| Equivalent noise field $B_b$ | 2.39 $\eta T$ |
| Emissive ability $P_e$ | 1.29 $mT/A$ |

## 4. MODELING

The model geometry is subdivided into two parts. The first part, $D_1$, contains the inspected specimen, a nickel-based alloy plate, noted by $\Omega_c$, which contains the rectangular slot (defect) $\Omega_d$. The second part, $D_2$, is the geometrical band containing the coil $\Omega_{t_0}$ where a uniform current density $\boldsymbol{j}_0$ is imposed. These two subdomains are separated by a lift-off, $D_0$. The moving band method is applied to take into account the displacement of the sensor. The Finite Element Method program is written using the developed ANSYS software in conjunction with MATLAB. Fig.3. shows the geometry of the considered problem.

The motion band method is used to ensure the displacement of the sensor along the conductive plate. This technique is based on a volumetric patching zone [22], [23]. The field of study is subdivided into three parts which represent the fixed and mobile parts and the air gap between the first two. This method was developed in 2D in the 1980s and then was taken up and improved. It consists of deforming the mesh at the movement band according to the position of the mobile part. Fig.4. is illustrating this technique. It consists of two steps:

Firstly, the geometrical band is created, during which the moving zone is subdivided into elementary regions of the identical length $\Delta x$. Then the geometry is all meshed.

Secondly, the regions corresponding to the sensor and the air are located in the geometrical band, and then the physical properties of the sensor and the air are assigned at each step displacement.
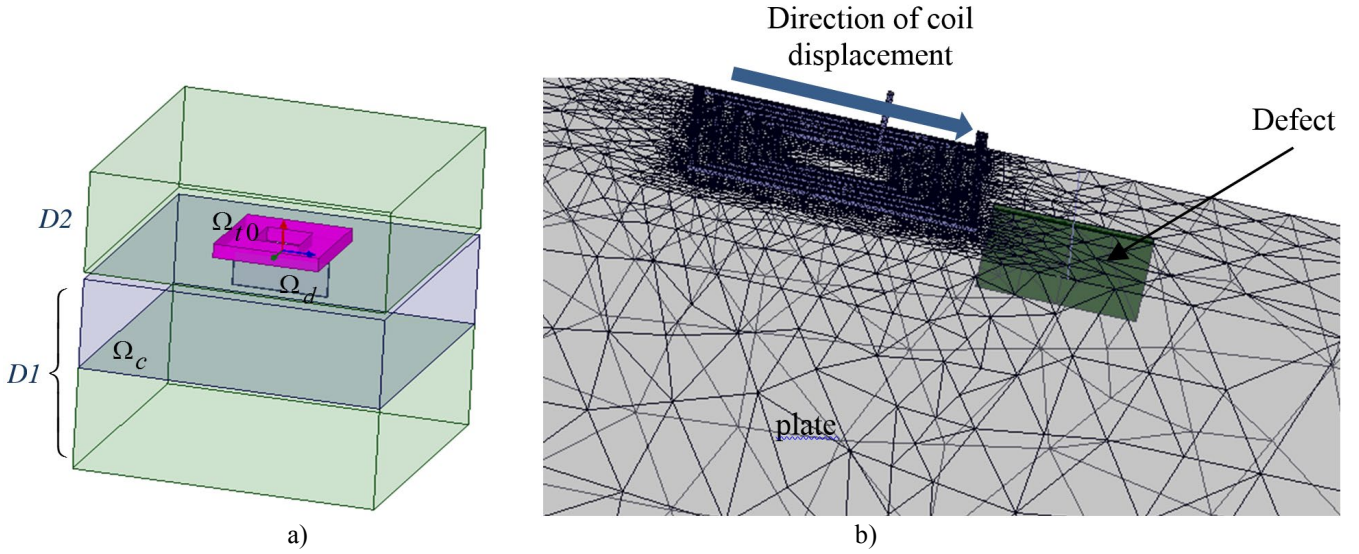
Fig.3. a) Description of the studied problem; b) 3-D mesh of the geometry.

During the movement of the mobile part, the elements of the movement band are deformed and the terms of the elementary matrix relating to the elements situated in the movement band are modified. To avoid obtaining bad quality elements in the movement band, when the displacement is greater than (length of an edge at the interface) the connectivities of the elements, in the movement band, switch between them.
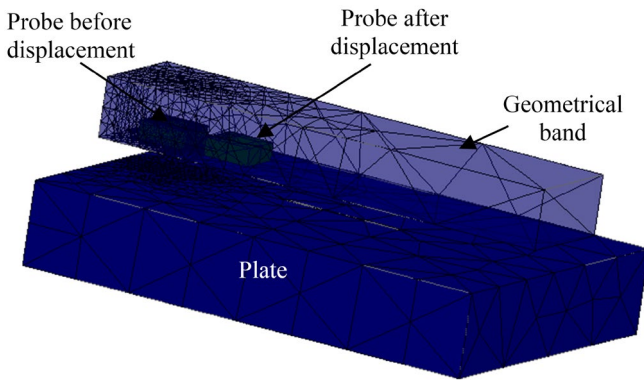


Fig.4. Moving band technique for sensor displacement.

## 5. DUAL FORMULATIONS FOR EDDY CURRENT PROBLEMS

Most three-dimensional finite element formulations of eddy current problems [24] can be classified into two dual formulations. One works with the variables of Ampere's law system, and the other uses the variables of Faraday's law system [25]. We will be interested in the two electric and magnetic formulations in combined potentials.

### A. Magnetic formulation

The magnetic field $h$ is then expressed by the sum of electric potential vectors $t$ and $t_0$ and the gradient of the magnetic scalar potential $\varphi$.

$$h = t + t_0 - grad\,\varphi \quad,$$
$$with \ \ n \times t\big|_{\Gamma_h} = 0 \ \ and \ \ \varphi\big|_{\Gamma_h} = 0, \tag{14}$$

such as $curl\,(t) = j$ and $curl\,(t_0) = j_0$, with $j$ and $j_0$ being the density of eddy currents and the density of current source. By introducing these equalities into the Faraday law and the flow conservation law, the system to solve is written as:

$$\begin{cases} div(\mu(t + t_0 - grad\varphi)) = 0 \ in \ \Omega \\ curl(\dfrac{1}{\sigma}curl\,t) + j\omega\mu(t - grad\varphi) = 0 in\Omega_c \end{cases}, \tag{15}$$

where $\omega$ is the current / voltage pulsation, $\mu = \mu_0.\mu_r$ ($\mu_0 = 4\pi10^{-7}$ H/m), $\mu_r$ is the relative permeability of the material used as inductor. The electric vector potential $t$ and the magnetic scalar potential in an element are then expressed by:

$$\varphi = \sum_{n=1}^{N_n} w_n \overline{\varphi_n} \tag{16}$$

$$t = \sum_{a=1}^{N_a} w_a \overline{t_a} \tag{17}$$

where $w_n$ is the vector of nodal shape functions, $\overline{\varphi_n}$ is the value of $\varphi$ at the $n^{th}$ node, $w_a$ is the vector of edge shape functions, and $\overline{t_a}$ is the circulation of $t$ along the $a^{th}$ edge. The matrix form of the system of equations is written as follows:

$$\begin{pmatrix} R_N & C_{AN} \\ C_{AN}^t & M_A + R_A \end{pmatrix} \begin{pmatrix} \Phi \\ T \end{pmatrix} = \begin{pmatrix} S \\ 0 \end{pmatrix},$$

$$with \quad \Phi = \begin{pmatrix} \overline{\varphi_1} \\ \cdot \\ \cdot \\ \overline{\varphi_{N_n}} \end{pmatrix} \quad T = \begin{pmatrix} \overline{t_1} \\ \cdot \\ \cdot \\ \overline{t_{N_a}} \end{pmatrix} \tag{18}$$

The system thus obtained is symmetrical and the matrix terms are:

$$\begin{cases} R_{N_{nm}} = j\omega \int_{\Omega} \mu\, \boldsymbol{grad} w_n \cdot \boldsymbol{grad} w_m\, d\Omega \\[2mm] C_{AN_{an}} = -j\omega \int_{\Omega_c} \mu\, \boldsymbol{grad} w_n \cdot w_a\, d\Omega \\[2mm] M_{A_{ab}} = j\omega \int_{\Omega_c} \mu\, w_a \cdot w_b\, d\Omega \\[2mm] R_{A_{ab}} = \int_{\Omega_c} \frac{1}{\sigma} \boldsymbol{curl}(w_a) \cdot \boldsymbol{curl}(w_b)\, d\Omega \\[2mm] S_m = j\omega \int_{\Omega_t} \mu\, \boldsymbol{grad}(w_m) \cdot t_0\, d\Omega \end{cases} \tag{19}$$

with:  $R_N$  the stiffness matrix of the nodes,
$R_A$  the stiffness matrix of the edges,
$M_A$  the mass matrix of the edges,
$C_{AN}$  the node-edge coupling matrix,
S  the source term.

The vectors $\Phi$ and $T$ contain the unknowns of the system which are, respectively, the values of the magnetic scalar potential at the nodes and the circulations of the electric vector potential along the edges of the mesh.

*B. Electric formulation*

The electric field $e$ can be expressed by the combination of the magnetic vector potential $a$ and electric scalar potential $\psi$ :

$$\begin{cases} e = -j\omega(a + \boldsymbol{grad}\psi) \; with \\ b = \boldsymbol{curl}\, a \end{cases} \tag{20}$$

The conduction current density $j$ is thus calculated:

$$\begin{aligned} j &= j_i + j_0 \\ &= -\sigma j\omega(a + \boldsymbol{grad}\psi) + \boldsymbol{curl}\, t_0 . \end{aligned} \tag{21}$$

Following the same procedure as for $t - \varphi$ formulation: The magnetic vector potential $a$ and the electric scalar potential $\psi$ are then expressed by:

$$\psi = \sum_{n=1}^{N_n} w_n \overline{\psi_n} \tag{22}$$

$$a = \sum_{a=1}^{N_a} w_a \overline{a_a} \tag{23}$$

In the same way as the $t - \varphi$ formulation, the magnetic vector potential $a$ is discretized by edge elements while the electric scalar potential $\psi$ is discretized by nodal elements. The system of equations is written within the matrix form:

$$\begin{pmatrix} R_N & C_{AN} \\ C_{AN}^t & M_A + R_A \end{pmatrix} \begin{pmatrix} \Psi \\ A \end{pmatrix} = \begin{pmatrix} 0 \\ S \end{pmatrix}$$

$$and \quad \Psi = \begin{pmatrix} \overline{\psi_1} \\ \cdot \\ \cdot \\ \overline{\psi_{N_n}} \end{pmatrix} \quad A = \begin{pmatrix} \overline{a_1} \\ \cdot \\ \cdot \\ \overline{a_{N_a}} \end{pmatrix} \tag{24}$$

The system thus obtained is symmetrical and the matrix terms are:

$$\begin{cases} R_{N_{nm}} = j\omega \int_{\Omega_c} \sigma\, \boldsymbol{grad} w_n \cdot \boldsymbol{grad} w_m\, d\Omega \\[2mm] C_{AN_{an}} = j\omega \int_{\Omega_c} \sigma\, w_a \cdot \boldsymbol{grad}\, w_m\, d\Omega \\[2mm] M_{A_{ab}} = j\omega \int_{\Omega} \sigma\, w_a \cdot w_b\, d\Omega \\[2mm] R_{A_{ab}} = \int_{\Omega} \frac{1}{\mu} \boldsymbol{curl}(w_a) \cdot \boldsymbol{curl}(w_b)\, d\Omega \\[2mm] S_b = \int_{\Omega_t} \boldsymbol{curl}(w_b) \cdot t_0\, d\Omega \end{cases} \tag{25}$$

The vectors $\Psi$ and $A$ are the unknowns of the system, respectively, the values of the electric scalar potential at the nodes and the circulations of the magnetic vector potential at the edges of the mesh.

## 6. EDDY CURRENT NDT RESULTS

Our study relies on the information from scans analysis, carried out by tiny displacements of the detector with 0.1 mm or 0.25 millimeter steps, parallel to the defect on the surface of the material. The resistance and reactance of the coil are calculated using the two formulations. The variation of the normalized resistance is given by: $\Delta R_n = (R - R_0)/X_0$, and the normalized reactance variation by: $\Delta X_n = (X - X_0)/X_0$, with $R, X$ the resistance and the reactance of the coil calculated in the presence of the conductive domain and $R_0$, $X_0$ the resistance and reactance of the coil in air (absence of the plate).

## A. Application I:

The parameters of the configuration are given in Table 2.

Fig.5. illustrates the distribution of eddy currents created by the coil. As can be seen in Fig.5.a), eddy current loops, generated at the surface of the conductive plate, are similar to the form of the coil. The current density is null within the defect zone as a result of the conductivity being zero, it is also very significant on the surface and it decreases gradually as we head to the bottom because of the skin effect as shown in Fig.5.b).

Table 2.  Dimensions of the problem.

| | |
|---|---|
| Turn width | 100 μm |
| Turn thickness | 25 μm |
| Gap between turns | 100 μm |
| Substrate thickness | 300 μm |
| Plate thickness | 3 mm |
| Plate conductivity | 0,76 MS/m |
| Relative permeability of the plate | 1 |
| Lift-off thickness | 50 μm |
| Excitation frequency | 800 kHz |
| Length of the flaw | 800 μm |
| Width of the flaw | 100 μm |
| Depth of the flaw | 400 μm |
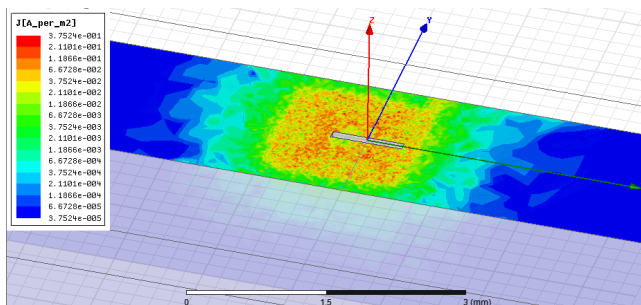


a)
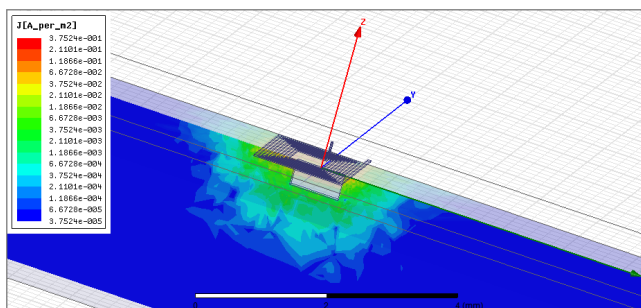


b)

Fig.5.  Eddy current distribution: a) Top view; b) Front view.

Fig.6.a) and Fig.6.b) present the variation of resistance and reactance as a function of the position of the symmetry axis of the coil relatively to the center of the flaw. The impedance real part (resistance) presents a trough curve and the imaginary part (reactance) presents a crest curve. It can be observed from the next figures, a good agreement between the FEM results issued from the magnetic and the electric formulation and the experimental results. These signals represent the signatures of the crack.
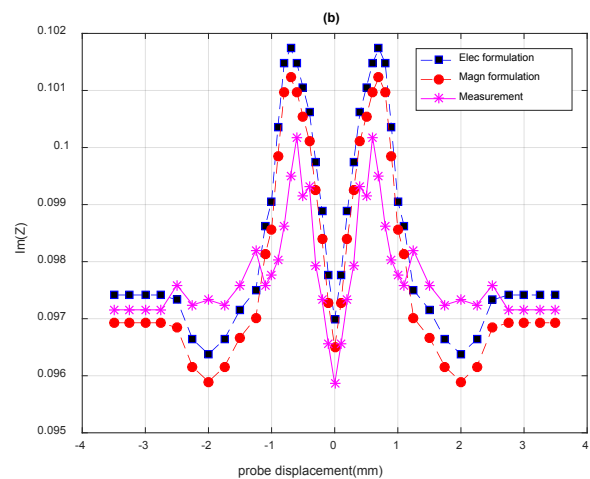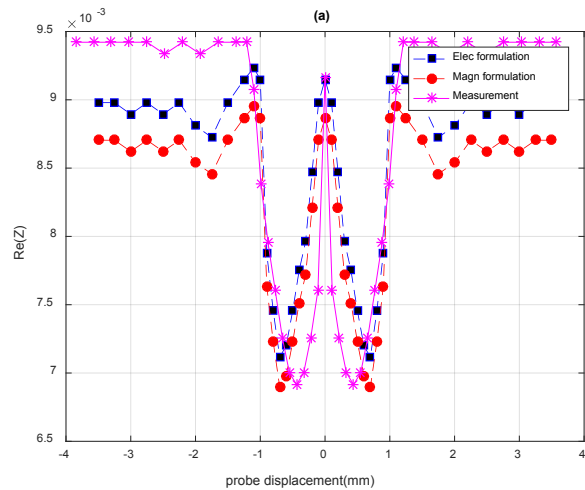




Fig.6. The variation of impedance of the system as function of displacement of the sensor: a) Impedance real part; b) Impedance imaginary part.

## B. Application II

The study of the effect of the crack dimensions on the EC signal allows us to define the sensitivity of the EC-NDT device. This sensitivity is decisive for knowing the parameters accessible by the inverse approach. Indeed, if a variation of an input parameter of the model is accompanied by a significant modification of the response, then we can say that the device is sensitive to this parameter and that it is possible to estimate the parameter in question.

### Crack length effect on EC signal

The influence of crack length on the sensor response is studied. The model used is the same one used for application

I, cracks of different lengths having the same width (0.1 mm) and depth (0.4 mm) are altered. Fig.7.a) and Fig.7.b) presents EC signatures of the resistance and reactance variations with respect to the sensor displacement produced by cracks having different lengths.
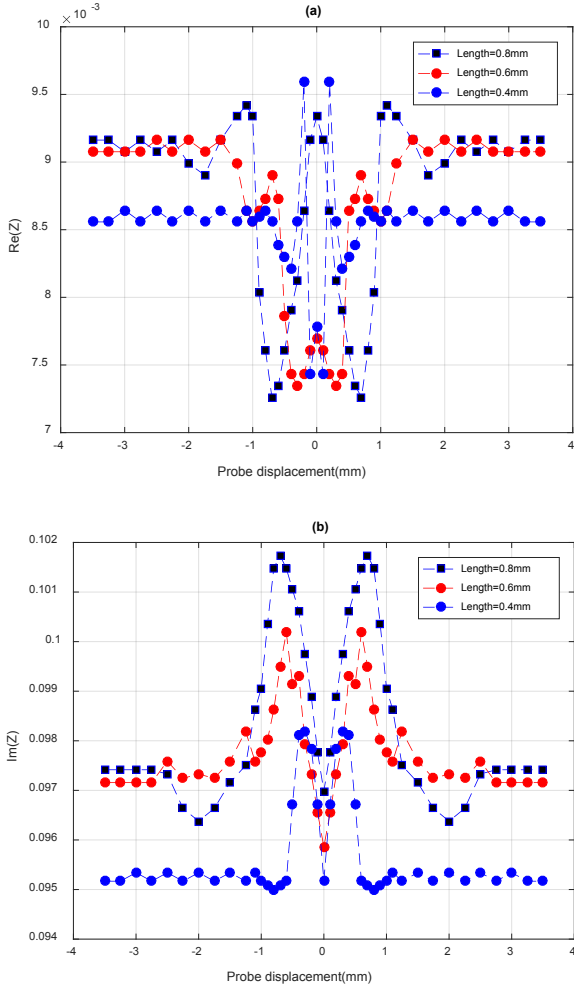


Fig.7. a) Impedance real part; b) Impedance imaginary part variation of cracks having different lengths.

As can be seen, for a variation of 100 % in the crack length (0.4 mm to 0.8 mm), we notice an increase in the variation of the normalized reactance from 0.098 to 0.102. As the length of the crack increases, the width of the curve increases and the maximum value of the response increases. It can be concluded that the EC sensor response strongly depends on the defect length. The micro-sensor is very sensitive to variations in the length of the defects.

*Crack depth effect on EC signal*

Next, the influence of crack depth on the sensor response is studied. The model used is the same one used for application I, cracks of different depths having the same length (0.8 mm) and width (0.4 mm) are altered. Fig.8.a) and Fig.8.b) show EC signatures of the impedance real part and imaginary part variations with respect to the sensor displacement produced by defects having different depths. As can be seen, for a depth variation of (0.1 mm to 0.4 mm), we observe an increase in the maximum variation of the normalized reactance from

0.098 to 0.102 and an increase in the curve width from (1.2 mm to 2.4 mm).

The variation of the crack depth influences the width of the curve and also the maximum value of the response of the sensor. So as the depth of the crack increases, the maximum value of the response increases and the width of the curve will be larger. It can be concluded that the EC signal for fine defects strongly depends on the defect depth. The micro-sensor is very sensitive to variations in the depth of the defects.
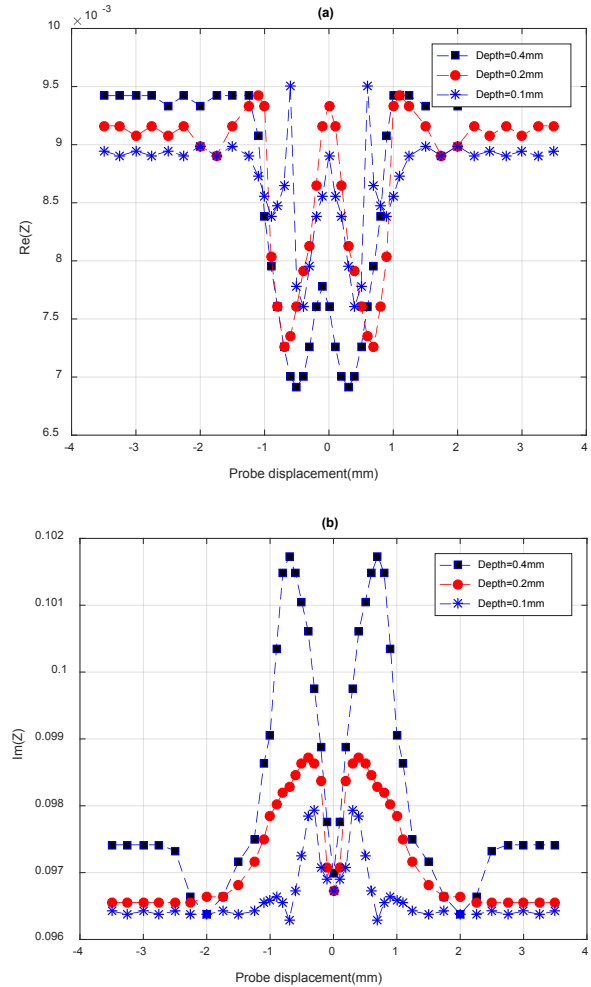


Fig.8. a) Impedance real part; b) Impedance imaginary part variation of cracks having different depths.

## 7. DATA INVERSION

This part is devoted to the characterization of cracks using the inversion technique. It constitutes the last link in the overall crack characterization strategy [18], [26]. After identification of the physical parameters and modeling of the crack, a database is thus built from the finite element results. A data inversion (crack depth and length), carried out by a neural network, allows us to completely characterize an emerging crack.

### A. RBF (Radial Basis Function) neural network:

RBF neural network is a feed-forward neural network [27]. The architecture of an RBF neural network consists of two

layers: a hidden layer and an output layer. The first layer consists of a number of elementary nodes that perform a nonlinear transformation of the input space. The second layer calculates a linear combination of the outputs of the elementary cores. It consists of a layer of scalar product type neurons with a linear activation function.

$f_1$: Gaussian activation function, $f_2$: Linear activation function.

The number of the hidden layer nodes is equal to the number of examples in the learning base. Moreover, the centers of the hidden layer nodes are identical to the values of input examples on the learning base.
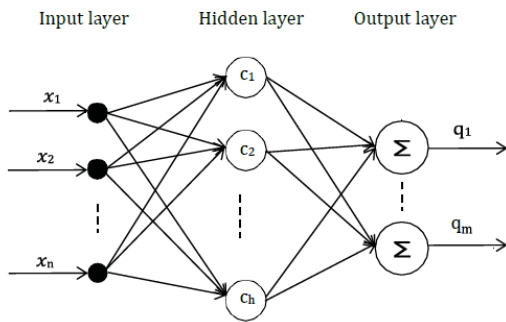


Fig.9. Network structure of RBF neural network.

*B. Result validation*

Once the learning phase is successfully completed, a test base is used. This database contains data belonging to the learning domain but different from the data used in the previous databases. On this basis, we test the ability of the network to estimate the output of the modeled real system when it is subjected to new inputs. In the last step, the network can be used to obtain the response to unknown input vectors, i.e. not encountered during learning, which constitutes the generalization phase. This ability to react correctly to unlearned input patterns (impedance variations) would give the neural networks an intrinsic robustness against faults occurring on the input pattern. The prediction model based on RBF neural network is established with the help of MATLAB neural network toolbox [28].

The relative error between the real and the estimated parameters is defined by the following relationship:

$$RE = \sqrt{\frac{1}{N}\sum_{i=1}^{N}\left(\frac{\widehat{q}_i - q_i}{q_i}\right)} \qquad (26)$$

Where $N$ is the number of examples on the test base, $q_i$ is the desired parameter (crack length or depth), and $\widehat{q}_i$ is the parameter estimated by the NN.

The results of inversion by RBF neural network for the evaluation of the length and the depth of crack are given by Fig.10.a) and Fig.10.b). There are good agreements between reconstructed and real crack parameters, thus it is possible to assume that the crack lengths and depths were estimated correctly, the reconstructed crack profiles are very close to the real ones.

Table 3. Relative errors by the RBF NN model.

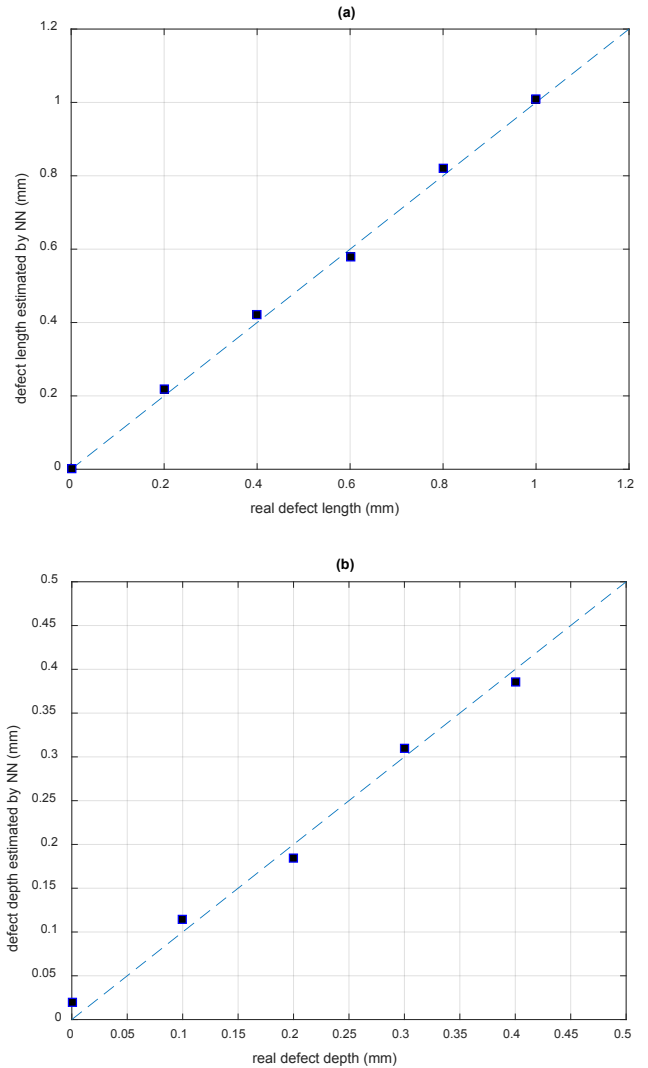| | Depth | Length |
|---|---|---|
| Relative error by RBF NN | 2.33 % | 2.25 % |



Fig.10. The performance of the RBF NN for the prediction of: a) the length; and b) the depth of the defect.

8. CONCLUSION

In this paper, we have shown the new possibilities offered by the miniaturization of eddy current sensors. An eddy current microsensor dedicated to the inspection of small surface defects is modeled in this paper using the finite element method giving a numerical resolution of Maxwell's equations in a 3D harmonic regime.

A new approach based on the motion band method for modeling the coil displacement in 3D plane along the conductive specimen is proposed; it can be concluded that:

- The motion band method allows efficient modeling for the displacement of the microsensor along the conductive plate without remeshing all the domains in each displacement;
- This method can take into account the presence of thin geometrical domains (the microcoil and the lift-off), it

leads to optimal storage, and ensures fast convergence of the system;

- The use of the microsensor provides high-quality inspection and better space resolution by miniaturization of their coils;
- The dimensions of the sensor conform it to the small geometry; it can also distinguish the different crack sizes;
- Geometric characteristics of the defects (length and depth) were estimated with good accuracy using RBF neural networks that were designed and implemented on the acquired EC signals.

REFERENCES

[1] Li, K., Li, L., Wang, P., Liu, J., Shi, Y., Zhen, Y., Dong, S. (2020). A fast and non-destructive method to evaluate yield strength of cold-rolled steel via incremental permeability. *Journal of Magnetism and Magnetic Materials*, 498, 166087. https://doi.org/10.1016/j.jmmm.2019.166087

[2] Velicheti, D., Nagy, P.B., Hassan, W. (2021). Residual stress and cold work assessment in shot-peened IN718 using a dual-mode electromagnetic technique. *NDT & E International*, 121, 102463. https://doi.org/10.1016/j.ndteint.2021.102463

[3] Obeidat, O., Yu, Q., Favro, L., Han, X. (2021). The effect of heating duration on the quantitative estimation of defect depth using sonic infrared imaging. *Journal of Nondestructive Evaluation, Diagnostics and Prognostics of Engineering Systems*, 4 (4), 044501. https://doi.org/10.1115/1.4050353

[4] Yu, Q., Obeidat, O., Han, X. (2018). Ultrasound wave excitation in thermal NDE for defect detection. *NDT & E International*, 100, 153-165. https://doi.org/10.1016/j.ndteint.2018.09.009

[5] Lu, M., Peyton, A., Yin, W. (2017). Acceleration of frequency sweeping in eddy-current computation. *IEEE Transactions on Magnetics*, 53 (7). DOI: 10.1109/TMAG.2017.2688326.

[6] Wendler, F., Munjal, R., Waqas, M., Laue, R., Härtel, S., Awiszus, B., Kanoun, O. (2021). Eddy current sensor system for tilting independent in-process measurement of magnetic anisotropy. *Sensors*, 21 (8), 2652. https://doi.org/10.3390/s21082652

[7] Chen, X., Lei, Y. (2015). Electrical conductivity measurement of ferromagnetic metallic materials using pulsed eddy current method. *NDT & E International*, 75, 33. https://doi.org/10.1016/j.ndteint.2015.06.005

[8] Li, K., Qiu, P., Wang, P., Lu, Z., Zhang, Z. (2021). Estimation method of yield strength of ferromagnetic materials based on pulsed eddy current testing. *Journal of Magnetism and Magnetic Materials*, 523, 167647. https://doi.org/10.1016/j.jmmm.2020.167647

[9] Lu, M., Meng, X., Chen, L., Huang, R., Yin, W., Peyton, A. (2020). Measurement of ferromagnetic slabs permeability based on a novel planar triple-coil sensor. *IEEE Sensors Journal*, 20 (6), 2904-2910. DOI: 10.1109/JSEN.2019.2957212.

[10] Zhang, H., Ma, L., Xie, F. (2019). A method of steel ball surface quality inspection based on flexible arrayed eddy current sensor. *Measurement*, 144, 192-202. https://doi.org/10.1016/j.measurement.2019.05.056

[11] Machado, M.A., Antin, K.-N., Rosado, L.S., Vilaca, P., Santos, T.G. (2019). Contactless high-speed eddy current inspection of unidirectional carbon fiber reinforced polymer. *Composites Part B: Engineering*, 168, 226-235. https://doi.org/10.1016/j.compositesb.2018.12.021

[12] Fava, J.O., Lanzani, L., Ruch, M.C. (2009). Multilayer planar rectangular coils for eddy current testing: Design considerations. *NDT & E International*, 42 (8), 713-720. https://doi.org/10.1016/j.ndteint.2009.06.005

[13] Mirzaei, M., Ripka, P., Chirtsov, A., Grim, V. (2020). Eddy current speed sensor with magnetic shielding. *Journal of Magnetism and Magnetic Materials*, 502, 166568. https://doi.org/10.1016/j.jmmm.2020.166568

[14] Mizukami, K., bin Ibrahim, A.S., Ogi, K., Matvieieva, N., Kharabet, I., Schulz, M., Heuer, H. (2019). Enhancement of sensitivity to delamination in eddy current testing of carbon fiber composites by varying probe geometry. *Composite Structures*, 226, 111227. https://doi.org/10.1016/j.compstruct.2019.111227

[15] Ye, C., Wang, Y., Wang, M., Udpa, L., Udpa, S.S. (2020). Frequency domain analysis of magnetic field images obtained using TMR array sensors for subsurface defect detection and quantification. *NDT & E International*, 116, 102284. https://doi.org/10.1016/j.ndteint.2020.102284

[16] Kuang, Y., Chew, Z.J., Ruan, T., Lane, T., Allen, B., Nayar, B., Zhu, M. (2021). Magnetic field energy harvesting from the traction return current in rail tracks. *Applied Energy*, 292, 116911. https://doi.org/10.1016/j.apenergy.2021.116911

[17] She, S., Chen, Y., He, Y., Zhou, Z., Zou, X. (2021). Optimal design of remote field eddy current testing probe for ferromagnetic pipeline inspection. *Measurement*, 168, 108306. https://doi.org/10.1016/j.measurement.2020.108306

[18] Mizukami, K., Watanabe, Y. (2018). A simple inverse analysis method for eddy current-based measurement of through-thickness conductivity of carbon fiber composites. *Polymer Testing*, 69, 320-324. https://doi.org/10.1016/j.polymertesting.2018.05.043

[19] Velicheti, D., Nagy, P.B., Hassan, W. (2019). Inversion procedure for dual-mode electromagnetic nondestructive characterization of shot-peened IN718. *NDT & E International*, 101, 17-28. https://doi.org/10.1016/j.ndteint.2018.09.013

[20] Meshkin, R., Maghsoodi, M., Saberkari, A., Niaboli-Guilani, M. (2013). High efficient CMOS class-E power amplifier with a new output power control scheme. *Journal of Electrical and Electronics Engineering*, 6 (1), 77-82.

[21] Madenci, E., Guven, I. (2015). *The Finite Element Method and Applications in Engineering Using ANSYS®*. Second Edition. Springer, ISBN 978-1-4899-7549-2.

[22] Sadowski, N., Lefevre, Y., Lajoie-Mazenc, M., Cros, J. (1992). Finite element torque calculation in electrical

machines while considering the movement. *IEEE Transactions on Magnetics*, 28 (2), 1410-1413. DOI: 10.1109/20.123957.

[23] Ren, Z. (1996). Auto-gauging of vector potential by iterative solver-numerical evidence. In *3rd International Workshop on Electric and Magnetic Fields*. AIM, 119-124.

[24] Ren, Z., Razek, A. (2000). Comparison of some 3D eddy current formulations in dual systems. *IEEE Transactions on Magnetics*, 36 (4), 751-755. DOI: 10.1109/20.877556.

[25] Ren, Z., Razek, A. (1996). Computation of 3-D electromagnetic field using differential forms based elements and dual formulations. *International Journal of Numerical Modelling*, 9 (1-2), 81-98.

[26] Le Bihan, Y., Pávó, J., Marchand, C. (2008). Characterization of small cracks in eddy current testing. *The European Physical Journal Applied Physics*, 43 (2), 231-237. https://doi.org/10.1051/epjap:2008112

[27] Wang, Z., Yang, B., Kang, Y., Yang, Y. (2016). Development of a prediction model based on RBF neural network for sheet metal fixture locating layout design and optimization. *Computational Intelligence and Neuroscience*, 2016, 7620438. https://doi.org/10.1155/2016/7620438

[28] Demuth, H., Beale, M. (2001). *Neural network toolbox: For use with MATLAB*. User's guide, Version 4. MathWorks, Inc.